

Topological Corner States in Bilayer and Trilayer Systems with Vertically Stacked Topologically Distinct Layers

Natsuko Ishida,^{1,*} Motohiko Ezawa,² Guangtai Lu,¹ Wenbo Lin,³
Yasutomo Ota,⁴ Yasuhiko Arakawa,⁵ and Satoshi Iwamoto^{1,6}

¹*Research Center for Advanced Science and Technology,
The University of Tokyo, 4-6-1 Komaba, Meguro-ku, Tokyo 153-8505, Japan*

²*Department of Applied Physics, The University of Tokyo,
7-3-1 Hongo, Bunkyo-ku, Tokyo 113-8656, Japan*

³*Institute of Innovative Research, Tokyo Institute of Technology,
2-12-1 Ookayama, Meguro-ku, Tokyo 152-8550, Japan*

⁴*Research Center for Department of Applied Physics and Physico-Informatics,
Keio University, 3-14-1 Hiyoshi, Kohoku-ku, Yokohama, Kanagawa 223-8522, Japan*

⁵*Institute for Nano Quantum Information Electronics,
The University of Tokyo, 4-6-1 Komaba, Meguro-ku, Tokyo 153-8505, Japan*

⁶*Institute of Industrial Science, The University of Tokyo,
4-6-1 Komaba, Meguro-ku, Tokyo 153-8505, Japan*

(Dated: June 14, 2024)

We investigate bilayer and trilayer systems composed of topologically distinct, vertically stacked layers based on the Benalcazar-Bernevig-Hughes model. We have identified a topological phase transition that significantly alters the number of the topological corner states in these systems. Additionally, we find that traditional nested Wilson loop analysis inaccurately classifies certain phases, leading us to evaluate multipole chiral numbers (MCNs) as a more appropriate topological invariant. This approach accurately identifies topological phases and the number of MCNs coincides with the number of corner modes, enhancing our understanding of topological insulators and opening avenues for further applications.

I. INTRODUCTION

Topological insulators are fascinating emerging materials found in condensed matter physics[1–3]. These materials are distinguished by their unique combination of an insulating bulk and metallic surfaces, i.e., edge states. The distinctive behavior of the edge states originates from the topological features in the bulk band structure giving a non-zero topological invariant, demonstrating the essential concept of bulk-boundary correspondence[4, 5]. The basic concept of topological materials has been expanded into classical wave phenomena, including photonics[6–10], acoustic waves[11–14], mechanical waves[15–18], thermal waves[19], as well as electric circuits[20–24]. This expansion has led to attractive applications such as topological lasers[25, 26].

Expanding beyond the conventional topological insulators, the concept of a higher-order topological insulators (HOTIs [27, 28]) has been proposed and is gaining significant attention. This class of materials is characterized by topological states that are at least two dimensions lower than the system itself. For instance, in a two-dimensional (2D) HOTI, one can observe zero-dimensional corner states.

Building on this framework, the majority of research has been directed towards the study of 2D monolayers[29–32] and their vertically stacked three-dimensional structures[33–38]. These investigations have

a broad scope, aiming to reveal the distinct topological properties intrinsic to these structures[39–41], as well as to examine their potential applications in diverse fields, including nanocavity lasers [42–44], nonlinear optics[45, 46], cavity quantum electrodynamics (QED) experiments[47, 48] and interferometer[49, 50]. There are some studies on vertically stacking of identical models in multilayer topological systems [51–53]. However, multilayer systems composed of topologically distinct layers have not been investigated.

In this paper, we investigate multilayer systems composed of topologically distinct layers. Our work is based on the Benalcazar-Bernevig-Hughes (BBH) model [27], a simplest model for studying quadrupole topological insulators. This model consists of π -flux square lattices and it supports topological corner modes. The realization of quadrupole insulators has been demonstrated through various experimental setups, including optical ring resonator arrays [54], waveguide arrays[55], electric circuits[21], acoustic system[56], and microwave resonator[57].

Our findings indicate a phase transition induced by the interlayer coupling, which significantly influences the emergence and annihilation of topological corner states. Interestingly, we identified a phase where the conventional method, using the nested Wilson loop, incorrectly classifies the phase as trivial, despite the presence of corner states. Therefore, we calculated a recently developed alternative topological invariant known as multipole chiral numbers (MCNs) [58] to evaluate the topological phases. Due to its capability to handle \mathbb{Z} -class higher-

* n-ishida@iis.u-tokyo.ac.jp

order topological systems, the MCN has begun to be applied across various models[59–62]. We found that the MCN precisely identifies the phases present in our model and accurately matches the number of corner modes at zero-energy. By adopting the MCN as a topological invariant, we not only identify changes in the number of corner modes but also uncover the phase transition induced by interlayer coupling.

II. TOPOLOGICAL CORNER STATES

The BBH lattice consists of four sites in a unit cell where the π -flux is inserted by introducing the negative coupling in a plaquette, as shown with the red bond in Fig. 1 (a). There are two topologically distinct phases, determined by the ratio of the intra-cell coupling to the inter-cell coupling. When the intra-cell coupling is weaker than inter-cell coupling, there exists four degenerate states that form a single set of corner modes, localized at each corner of the structure within a band gap at energy $E = 0$. The bulk Hamiltonian for the system shown in Fig. 1 (a) is given by

$$\mathcal{H}_{\text{BBH}}(k_x, k_y) = \begin{pmatrix} 0 & 0 & -(\kappa_1 + \kappa_2 e^{-ik_x}) & \kappa_1 + \kappa_2 e^{-ik_y} \\ 0 & 0 & \kappa_1 + \kappa_2 e^{ik_y} & \kappa_1 + \kappa_2 e^{ik_x} \\ -(\kappa_1 + \kappa_2 e^{ik_x}) & \kappa_1 + \kappa_2 e^{-ik_y} & 0 & 0 \\ \kappa_1 + \kappa_2 e^{ik_y} & \kappa_1 + \kappa_2 e^{-ik_x} & 0 & 0 \end{pmatrix}. \quad (1)$$

Throughout this paper, we use κ_1 (κ_2) and κ_2 (κ_1) as the intra-cell and inter-cell couplings for the topological (trivial) system, respectively, with its corresponding Hamiltonian $\mathcal{H}_{\text{BBH}}^{\text{Topo}}(k_x, k_y)$ ($\mathcal{H}_{\text{BBH}}^{\text{Tri}}(k_x, k_y)$). Here, we suppose $\kappa_1 < \kappa_2$, and both are positive.

The BBH system has two occupied degenerate bands that possess two cancelling dipole moments and a non-vanishing quadrupole moment. By adapting the Wilson loop calculation, the degeneracy is lifted, resulting in two distinct single-band subspaces where Wannier bands become non-degenerate. Consequently, each Wannier band carries its own topological invariant, which can be obtained through the nested Wilson loop calculation [27]. Following the calculation, a quadrupole moment $q_{xy} = \frac{1}{2}$ signifies that the system is topological, while $q_{xy} = 0$ signifies that the system is trivial.

In our study, we consider a vertically stacked configuration composed of topologically distinct layers, taking into account the vertical nearest-neighbor site coupling denoted by t_v . Fig. 1 (b) illustrates the considered BBH bilayer system and its unit cell, where the top and bottom layers are topological and trivial, respectively. For trilayer systems, we consider two cases as shown in Figs. 1 (d) and (e), where the arrangements of the topological and trivial layers are flipped.

A. Topological corner states in BBH bilayer lattice

The Hamiltonian describing the bilayer system, shown in Fig. 1 (b), is given by

$$\mathcal{H}_{\text{bilayer}} = \begin{pmatrix} \mathcal{H}_{\text{BBH}}^{\text{Topo}} & \mathcal{H}_v \\ \mathcal{H}_v & \mathcal{H}_{\text{BBH}}^{\text{Tri}} \end{pmatrix}, \quad (2)$$

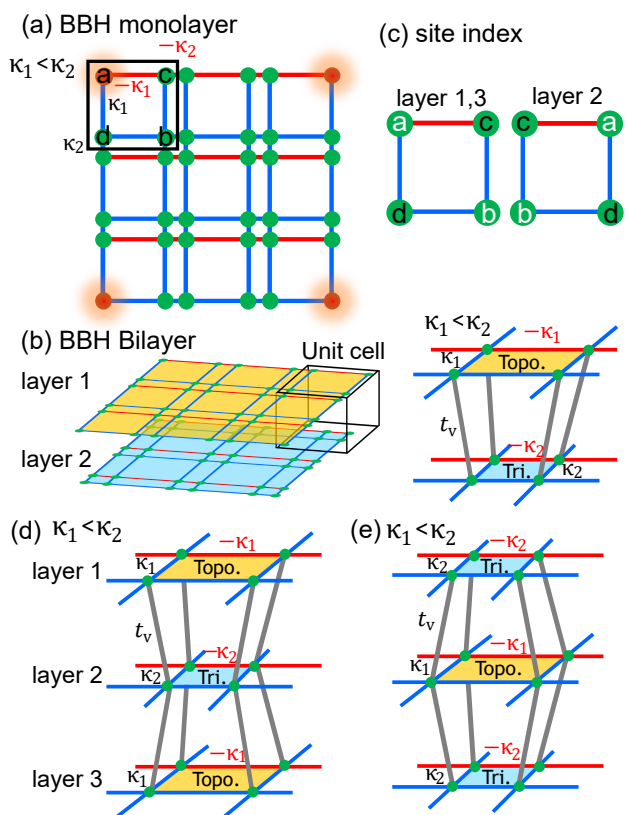


FIG. 1. (a) Blue and red bonds represent the positive and negative couplings, respectively. Corner states, shown in red at each corner, appear when $\kappa_1 < \kappa_2$. (b) An illustration of the BBH bilayer system composed of topological and trivial layers. κ_1 (κ_2) and κ_2 (κ_1) denote the intra- and inter-cell couplings for topological (trivial) system, respectively. (c) The labeling lattice sites a, b, c, and d represent the Hamiltonian basis for each layer. (d,e) Two distinct BBH trilayer systems where topologically distinct layers are stacked on top of each other.

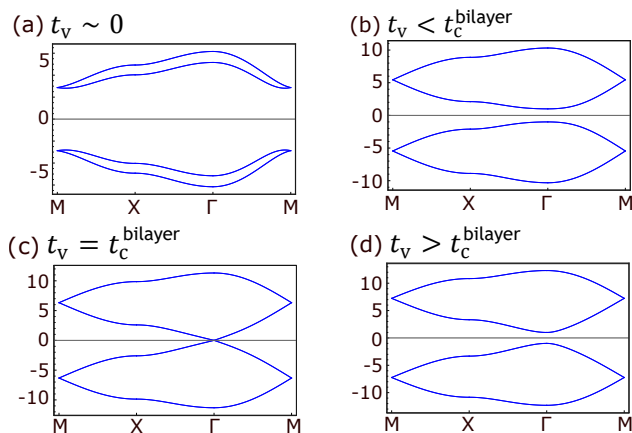


FIG. 2. Interlayer coupling t_v dependence of band structures for BBH bilayer system where top and bottom layers are composed of two topologically distinct layers. Parameters are chosen as (a) $t_v=0.5$, (b) $t_v = t_c^{\text{bilayer}} - 1$, (c) $t_v = t_c^{\text{bilayer}}$, (d) $t_v = t_c^{\text{bilayer}} + 1$, $\kappa_1=1$, and $\kappa_2=3$. $t_c^{\text{bilayer}} (= 4\sqrt{2})$ denotes the critical value where a band gap closes.

where

$$\mathcal{H}_v = t_v \begin{pmatrix} 0 & 0 & 1 & 0 \\ 0 & 0 & 0 & 1 \\ 1 & 0 & 0 & 0 \\ 0 & 1 & 0 & 0 \end{pmatrix} = t_v \sigma_x \otimes \mathbb{I}_2. \quad (3)$$

Here, we use the site index shown in Fig. 1(c) in which chiral symmetry is preserved. This ordering is essential for the theoretical analysis presented later in this paper. σ_x and \mathbb{I}_2 are Pauli matrix and two by two identical matrix, respectively. The band structure has four pairs of doubly degenerate bands, and exhibits both opening and closing of a band gap, around the Γ point as t_v changes. (Fig. 2). The critical value t_c^{bilayer} corresponds to the point at which the band gap closes, defined as $t_c^{\text{bilayer}} = \sqrt{2}(\kappa_1 + \kappa_2)$. See appendix A for details.

We now consider a finite BBH model with square geometry, with each layer forming a BBH lattice consisting of $2N \times 2N$ sites. Fig. 3(a) shows the energy spectrum as a function of varying t_v . In the weak interlayer coupling regime ($t_v < t_c^{\text{bilayer}}$), the system possesses a single set of corner modes, consisting of a total of four degenerate states, each predominantly localized at the corners of the layers. These are depicted by the red line in the figure. Fig. 3(b) shows the field amplitude of the corner state, summed over for all four states. Notably, these corner states disappear when the interlayer coupling exceeds the critical value t_c^{bilayer} . Sudden disappearance of the corner states, accompanied by a gap closing, suggests a topological phase transition associated with increasing interlayer coupling strengths.

In order to determine the topological phases, we calculate the quadrupole moment q_{xy} [27] via the nested Wilson loop. As a result, we find that $q_{xy} = \frac{1}{2}$ for $t_v < t_c^{\text{bilayer}}$, identifying the system as topological, while

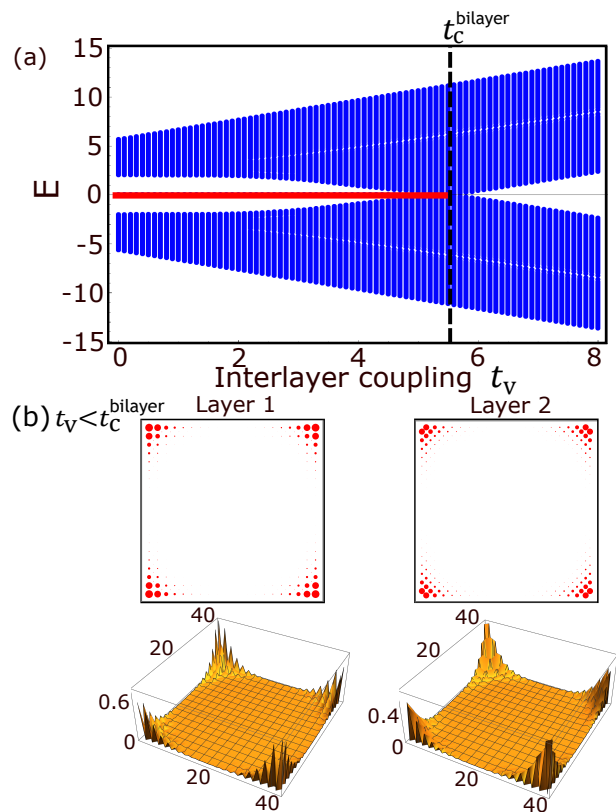


FIG. 3. (a) Energy spectrum vs t_v for BBH bilayer system. Blue dots represent the bulk spectrum, with or without gapped edges, whereas the red line corresponds to a single set of corner modes. The gapped edge states appear when corner modes exist. (b) Field amplitude summed over the four corner modes at $E = 0$ for $t_v = t_c^{\text{bilayer}} - 1$. Parameters are chosen as $\kappa_1=1$, $\kappa_2 = 3$ and $N = 20$.

$q_{xy} = 0$ for $t_v > t_c^{\text{bilayer}}$, indicating a trivial phase. These results indicate that the interlayer coupling induces a topological phase transition in the BBH bilayer system. The presence and absence of topological corner states change at the critical value t_c^{bilayer} bilayer as the band gap closes and re-opens. This critical value marks the transition point where the number of topological corner states changes. The detailed calculation of the quadrupole moment is shown in the Appendix B.

B. Topological corner states in BBH trilayer lattice

We proceed to study a BBH trilayer system depicted in Fig. 1(d). This arrangement consists of a trivial layer positioned between two topological layers, where the layers are coupled by an interlayer coupling t_v .

The system Hamiltonian is given by

$$\mathcal{H}_{\text{trilayerI}} = \begin{pmatrix} \mathcal{H}_{\text{BBH}}^{\text{Topo}} & \mathcal{H}_v & 0 \\ \mathcal{H}_v & \mathcal{H}_{\text{BBH}}^{\text{Tri}} & \mathcal{H}_v \\ 0 & \mathcal{H}_v & \mathcal{H}_{\text{BBH}}^{\text{Topo}} \end{pmatrix}, \quad (4)$$

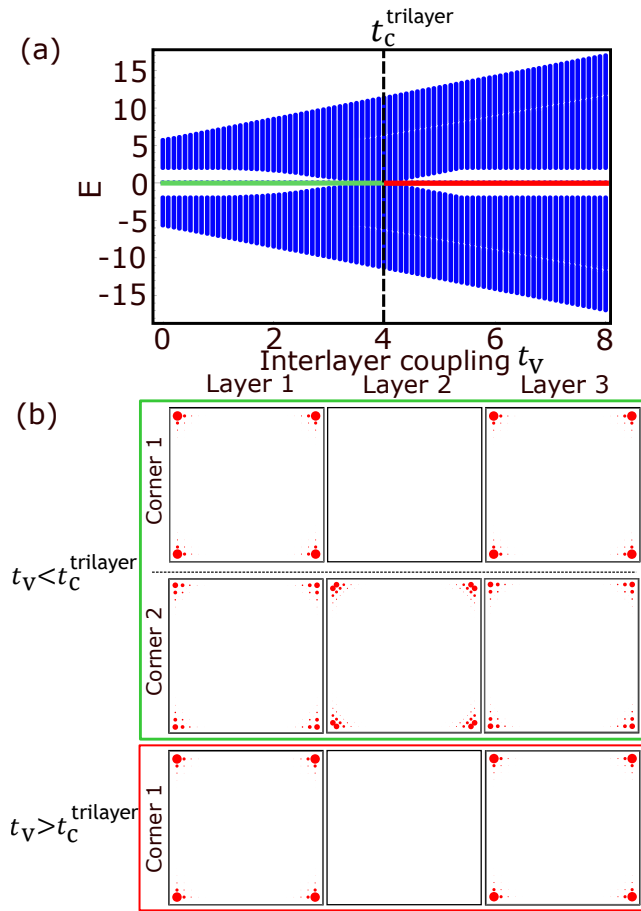


FIG. 4. (a) Energy spectrum vs t_v for BBH trilayer system (topological-trivial-topological structure). Blue dots represent the gapped edge states and bulk spectrum. The green and red lines correspond to four and a single set of corner modes, respectively. (b) Field amplitude summed over the four corner modes at $E = 0$ for $t_v = t_c^{\text{trilayer}} - 1$ and $t_v = t_c^{\text{trilayer}} + 1$. 'Corner 1' persists even after exceeding the critical value, while 'corner 2' vanishes at the critical value t_c^{trilayer} . Parameters are chosen as $\kappa_1=1$, $\kappa_2 = 3$, and $N = 20$.

with the interlayer coupling matrix \mathcal{H}_v . Similar to the bilayer system, the labeling of sites in the Hamiltonian varies between odd and even layers to maintain the chiral symmetry, as shown in Fig. 1(c). This labeling is crucial for applying the methods we will discuss in the next section. The trilayer system possesses six pairs of doubly degenerate bands. Analogous to the bilayer system, band gap closes at a critical value $t_c^{\text{trilayer}} = \kappa_1 + \kappa_2$ (See appendix A). The band gap re-opens again when t_v exceeds the critical value.

For a finite BBH trilayer system with square geometry, with each layer consisting of $2N \times 2N$ sites, we calculate the eigenenergies as a function of the interlayer coupling strength (Fig 4(a)). When $t_v < t_c^{\text{trilayer}}$, which is below the critical value, there are two sets of corner states, with a total number of eight (illustrated by the green line in the figure). In contrast, when t_v exceeds t_c^{trilayer} , only a

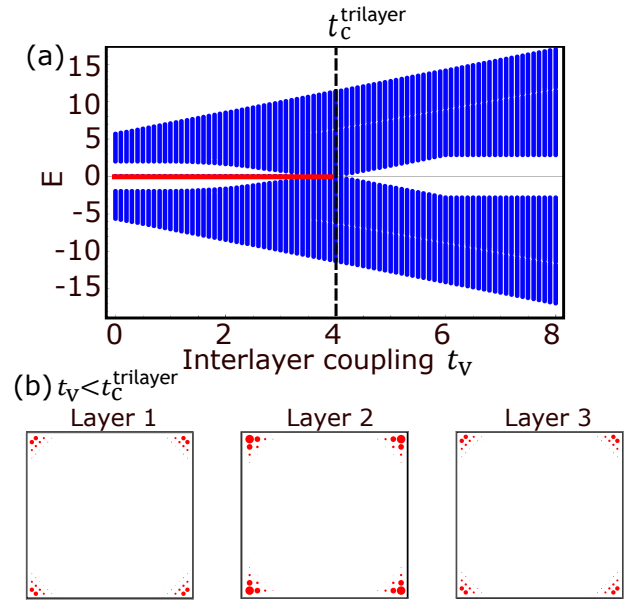


FIG. 5. (a) Energy spectrum vs t_v for BBH trilayer system (trivial-topological-trivial structure). Blue dots correspond to the bulk spectrum, with or without gapped edges, whereas the red line represents a single set of corner modes. Gapped edges are present when the system exhibits corner states. (b) Field amplitude summed over the four corner modes at $E = 0$ for $t_v = t_c^{\text{trilayer}} - 1$. Parameters are chosen as $\kappa_1=3$, $\kappa_2 = 1$ and $N = 20$.

single set of corner states survives, with a total number of four (indicated by the red line). Each of these sets consists of four degenerate modes located at $E = 0$. These two sets of corner states are distinguished by their unique field distributions (Fig. 4 (b)). Specifically, the corner states that disappear at the critical interlayer coupling show non-zero field amplitudes across all layers, which corresponds to symmetric coupling between the corners (corner 2). Conversely, the corner states that remain after exceeding the critical interlayer coupling exhibit a complete absence of field amplitude in the middle layer, which corresponds to anti-symmetric coupling between the corners (corner 1). The presence of topological corner states, 'Corner 1', at large interlayer couplings, is understood by an effective model in the vicinity of the zero-energy, derived based on the perturbation theory. See Appendix C.

As discussed in the subsection II.A of the bilayer system, we calculate the quadrupole moment q_{xy} to identify the topological phases of the trilayer system. Consequently, our analysis shows that $q_{xy} = 0$ for $t_v < t_c^{\text{trilayer}}$, classifying the system as trivial, despite the presence of two sets of corner states at $E = 0$. In the case where $t_v > t_c^{\text{trilayer}}$, we have $q_{xy} = \frac{1}{2}$, indicating the system as topological. This leads to the issue where the quadrupole moment fails to fully capture the topological phases in certain instances. Therefore, the introduction of another invariant is essential to accurately describe the topologi-

cal phases of both bilayer and trilayer BBH systems. We will calculate and discuss this alternative invariant in the next section.

Next, we study a trilayer system which involves a topological layer sandwiched between two trivial layers, with each layer coupled by an interlayer coupling t_v . This arrangement is depicted in Fig. 1 (e). In this case, the Hamiltonian is given by

$$\mathcal{H}_{\text{trilayerII}} = \begin{pmatrix} \mathcal{H}_{\text{BBH}}^{\text{Tri}} & \mathcal{H}_v & 0 \\ \mathcal{H}_v & \mathcal{H}_{\text{BBH}}^{\text{Topo}} & \mathcal{H}_v \\ 0 & \mathcal{H}_v & \mathcal{H}_{\text{BBH}}^{\text{Tri}} \end{pmatrix}. \quad (5)$$

Its critical value is determined by $t_c^{\text{trilayer}} = \kappa_1 + \kappa_2$, which is identical to that in the previous trilayer case.

Fig. 5(a) shows the energy spectrum as a function of t_v . There is a single set of corner modes that includes four degenerate corner states at $E = 0$ (depicted by the red line) when $t_v < t_c^{\text{trilayer}}$; however, all corner modes disappear above the critical value t_c^{trilayer} . The field amplitudes of the corner modes, shown in Fig. 5 (b), are distributed across each layer. The quadrupole moments are obtained as $q_{xy} = \frac{1}{2}$ for $t_v < t_c^{\text{trilayer}}$, identifying the phase as topological, while $q_{xy} = 0$ for $t_v > t_c^{\text{trilayer}}$, classifying it as trivial. We note that in BBH trilayer systems with large interlayer coupling t_v , the size of the band-gap varies between two distinct systems, despite them having identical band structures, as shown in Figs 4(a) and 5(a). This discrepancy arises due to the presence of gapped edge states within the band gap as illustrated in Fig. 4(a).

III. 2D WINDING NUMBER IN REAL SPACE

As we observed a discrepancy between the quadrupole moment and the presence of corner states when

$$|\psi\rangle^T = (a_1^1, \dots, a_{N^2}^1, b_1^1, \dots, b_{N^2}^1, a_1^2, \dots, a_{N^2}^2, b_1^2, \dots, b_{N^2}^2, c_1^1, \dots, c_{N^2}^1, d_1^1, \dots, d_{N^2}^1, c_1^2, \dots, c_{N^2}^2, d_1^2, \dots, d_{N^2}^2).$$

Superscripts represent the layer index, where layer 1 and 2 correspond to upper and lower layer, respectively. The quadrupole moment operator for the BBH bilayer system is represented by a following sublattice quadrupole moment operator[58, 64]

$$Q_{xy}^S = \sum_{\mathbf{R}, \alpha \in S} e^{-i \frac{2\pi xy}{N^2}} |\mathbf{R}, \alpha\rangle \langle \mathbf{R}, \alpha| \quad (7)$$

for $S = A, B$. Each layer consists of $N \times N$ unit cells, each labeled as $\mathbf{R} = (x, y)$. We diagonalize the Hamiltonian $\mathcal{H}_{\text{bilayer}}$ by using the singular value decomposition (SVD) of $h_{\text{bilayer}} = U_A \Sigma U_B^\dagger$, where U_A (U_B) denotes a $4N^2 \times 4N^2$ unitary matrix while Σ is a diagonal matrix of singular values. Using $\hat{Q}_{xy}^S = U_S^\dagger Q_{xy}^S U_S$, the MCN is

$t_v < t_c^{\text{trilayer}}$, in the trilayer case ('topological-trivial-topological' structure), we need to calculate another topological invariant to discuss its topological phase in detail. We choose the MCN as the additional invariant, which is capable of accurately evaluating the topological phases of \mathbb{Z} -class chiral-symmetric higher-order topological systems, as recently introduced by [58]. The MCNs are analogous to the 2D winding number in real space, based on the work described in Ref.[63]. This development is especially crucial in situations where existing theoretical frameworks, such as the nested Wilson loop, may erroneously categorize certain phases as trivial. The MCN provides an innovative approach for analyzing these systems. Notably, the value of MCN directly correlates with the number of degenerate zero-energy corner states present in a finite system, thereby offering a more precise invariant for examining these unique topological states. In this study, we use the MCNs to identify the topological phases of both BBH bilayer and trilayer systems in their chiral-symmetric forms. This is particularly relevant in cases where the conventional nested Wilson approach inaccurately classified the phase as trivial, despite the presence of zero-energy corner states.

To compute the topological invariant for BBH bilayer system, we modify the Hamiltonian in its chiral-symmetric form for its finite-size system as follows:

$$\mathcal{H}_{\text{bilayer}} = \begin{pmatrix} 0 & h_{\text{bilayer}} \\ h_{\text{bilayer}}^\dagger & 0 \end{pmatrix}, \quad (6)$$

Note that the labeling of sites in the Hamiltonian differs between layer 1 and layer 2 in order to preserve the chiral symmetry, as shown in Fig. 1(c). Also, sites a and b belong to sublattice A, while sites c and d belong to sublattice B. When a 2D square-lattice has N unit cells in the x and y -directions (i.e. each layer consists of $N \times N$ unit cells), h_{bilayer} is a $4N^2 \times 4N^2$ matrix. Here, the eigenstates of $\mathcal{H}_{\text{bilayer}}$ in equation (6) are denoted as

defined as [58]

$$N_{xy} = \frac{1}{2\pi i} \text{Tr} \left[\log(\hat{Q}_{xy}^A \hat{Q}_{xy}^{B\dagger}) \right]. \quad (8)$$

Our calculations reveal that the MCN invariant is $N_{xy} = 1$ for $t_v < t_c^{\text{bilayer}}$ while $N_{xy} = 0$ for $t_v > t_c^{\text{bilayer}}$, where the MCN number matches the number of corner states at $E = 0$. This result is consistent with the Wilson loop calculation. The comprehensive calculations for MCNs are presented in the Appendix D. It is important to note that to calculate the topological invariant, sufficiently large systems are required.

This calculation can readily be adapted for trilayer cases. First, we rewrite the trilayer Hamiltonian in equation (4) and (5) into a form that preserves chiral symme-

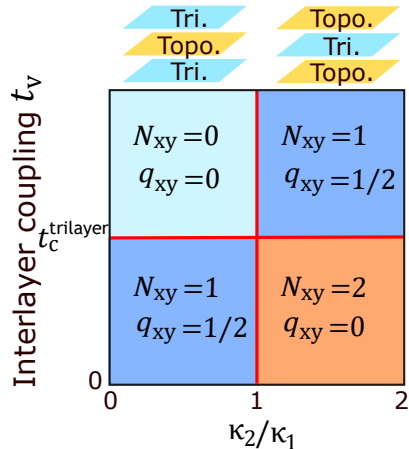


FIG. 6. Topological phase diagram of the BBH trilayer system as a function of the coupling strengths ratio and the interlayer coupling, highlighting areas defined by distinct multipole chiral numbers N_{xy} and quadrupole moments q_{xy} . The closing of band gaps is marked by red solid lines.

try, given by

$$\mathcal{H}_{\text{trilayer}} = \begin{pmatrix} 0 & h_{\text{trilayer}} \\ h_{\text{trilayer}}^\dagger & 0 \end{pmatrix}. \quad (9)$$

The Hamiltonian h_{trilayer} is represented by a matrix of size $6N^2 \times 6N^2$. By using the quadrupole moment operators in equation (7), we obtain the MCN, given by equation (8). For a trilayer system depicted in Fig. 1(d), the invariant is obtained as $N_{xy} = 2$ for $t_v < t_c^{\text{trilayer}}$ while $N_{xy} = 1$ for $t_v > t_c^{\text{trilayer}}$. The MCN number perfectly matches the number of corner states at $E = 0$. Similarly, for the alternative trilayer system illustrated in Fig. 1(e), we obtain $N_{xy} = 1$ for $t_v < t_c^{\text{trilayer}}$ and $N_{xy} = 0$ for $t_v > t_c^{\text{trilayer}}$, which again coincides with the number of corner states at $E = 0$. Therefore, we conclude that the MCN accurately captures the topological phases that even the quadrupole moment may fail to identify.

IV. DISCUSSION AND CONCLUSIONS

We investigated bilayer and trilayer BBH structures, constructed by stacking topologically distinct layers. By adjusting the interlayer coupling strengths, we identified changes in the number of corner modes, indicating a topological phase transition. This topological phase transition, accompanied by band gap closing, is induced by the interlayer coupling.

To identify the topological phases, we first calculated the quadrupole moments using the nested Wilson loop approach, a well-known method for analyzing quadrupole insulators. The quadrupole moments explained the topological phases of BBH bilayer and 'trivial-topological-

trivial' trilayer structures. However, we observed a mismatch between the quadrupole moments and the presence of corner modes in 'topological-trivial-topological' trilayer structure when the interlayer coupling was below the critical value. In contrast, MCNs, which are a topological invariant for \mathbb{Z} -class chiral-symmetric higher-order topological systems recently reported, can systematically explain the results. We also confirmed that the number of corner states coincides with the MCNs across all interlayer coupling regimes for all three structures we considered. As we identified a topological phase that may have been misclassified as trivial when analyzed through the conventional nested Wilson loop approach, this finding highlights the need for the topological invariant, the MCN, as a more appropriate method of evaluating \mathbb{Z} -class higher-order topological systems.

The categorizing the phase transition induced by the interlayer coupling is below:

Bilayer (topological-trivial):

from the topological phase with $N_{xy} = 1$ to the trivial phase with $N_{xy}=0$.

Trilayer (topological-trivial-topological):

from the topological phase with $N_{xy} = 2$ to the topological phase with $N_{xy} = 1$.

Trilayer (trivial-topological-trivial):

from the topological phase with $N_{xy} = 1$ to the trivial phase with $N_{xy}=0$.

Figure 6 displays the topological phase diagram, which illustrates both the MCNs and the quadrupole moments in BBH trilayer systems.

This study demonstrates that adjusting the interlayer coupling manipulates the topological phase transition, which is accompanied by the appearance and disappearance of corner modes, potentially expanding the scope of applications. The configuration of vertically stacking layers, as discussed in our study, can be implemented in existing platforms, such as electrical circuits. Additionally, the field distribution of corner modes suggests that the intensity of corner modes can be accumulated through stacked layers, which can be adapted to develop a novel topological laser. We believe that our findings provide valuable insights into the manipulation of localized modes within multilayer systems, opening avenues for innovative device engineering.

APPENDIX A: BULK ENERGY FOR THE BBH BILAYER AND TRILAYER SYSTEM

(i) The bulk spectrum of the bilayer system $\mathcal{H}_{\text{bilayer}}$ is obtained as

$$E = \pm \sqrt{2F + t_v^2 \pm \sqrt{2G}}, \quad (10)$$

with

$$F = \kappa_1^2 + \kappa_2^2 + \kappa_1 \kappa_2 (\cos k_x + \cos k_y), \quad (11)$$

$$G = (\kappa_1 + \kappa_2)^2 t_v^2 (\cos k_x + \cos k_y + 2), \quad (12)$$

where each energy is two-fold degenerated. At the Γ point, the energy is obtained as

$$E = \pm\sqrt{2}|\kappa_1 + \kappa_2| \pm t_v. \quad (13)$$

The gap closes at

$$t_v = \pm\sqrt{2}(\kappa_1 + \kappa_2). \quad (14)$$

(ii) The bulk spectrum of the trilayer systems $\mathcal{H}_{\text{trilayerI}}$ and $\mathcal{H}_{\text{trilayerII}}$ is obtained as

$$E = \pm\sqrt{2}\sqrt{F}, \quad \pm\sqrt{2}\sqrt{F + t_v^2 \pm \sqrt{G}}, \quad (15)$$

where each energy is two-fold degenerated. It is remarkable that the bulk spectrum is identical between $\mathcal{H}_{\text{trilayerI}}$ and $\mathcal{H}_{\text{trilayerII}}$. At the Γ point, the energy is obtained as

$$E = \pm\sqrt{2}|\kappa_1 + \kappa_2|, \quad \pm\sqrt{2}(\kappa_1 + \kappa_2 \pm t_v). \quad (16)$$

The gap closes at

$$t_v = \pm(\kappa_1 + \kappa_2). \quad (17)$$

APPENDIX B: QUADRUPOLE MOMENT q_{xy} IN BBH SYSTEM

In the BBH model, the bulk quadrupole moment q_{xy} , its boundary polarizations $p_{x,y}$ and corner charges Q have the following relationship: $|p_x^{\text{edge}\pm y}| = |p_y^{\text{edge}\pm x}| = |Q^{\text{corner}\pm x, \pm y}| = |q_{xy}|$ [27]. The requirements for quantizing the quadrupole moment q_{xy} are existence of three symmetries, which are inversion symmetry and x, y -reflection symmetry under a gauge transformation. These constraints lead to quantized values of the Wannier band polarizations $p_y^{\pm}, p_x^{\pm} \stackrel{\mathcal{I}, \mathcal{M}_x, \mathcal{M}_y}{=} 0$ or $1/2$. Furthermore, when the system preserves C_4 symmetry, the classification of the Wannier bands is \mathbb{Z}_2 [33]. Therefore, the quadrupole moment q_{xy} can be described by $q_{xy} = p_y^{\pm} = p_x^{\pm} = 0$ or $1/2$ and the topological invariant is defined by the polarizations which are obtained as follows:

$$p_y^{\pm} = -\frac{i}{2\pi} \frac{1}{N_x} \sum_{k_x} \log[\tilde{W}_{y,k_x}^{\pm}] = 0 \text{ or } \frac{1}{2} \quad (18)$$

where \tilde{W}_{y,k_x}^{\pm} is a nested Wilson loop along k_y [27]. The quadrupole moment of $\frac{1}{2}$ and 0 imply that the system is topological and trivial, respectively.

By adapting the Wilson loop calculation to the occupied bands of the BBH bilayer shown in Fig. 2, we obtain four non-degenerate Wannier bands, as depicted in

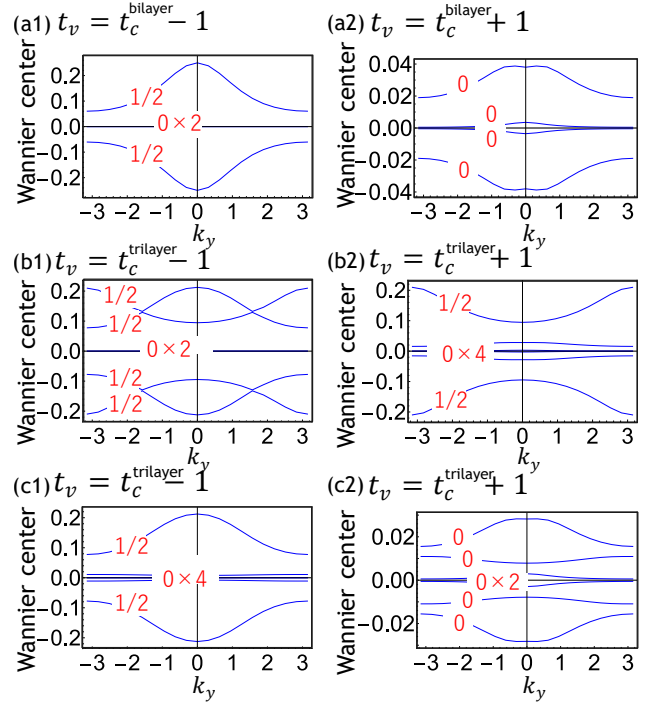


FIG. 7. Wannier bands of (a) BBH bilayer, (b) 'Topological-Trivial-Topological' BBH trilayer systems and (c) 'Trivial-Topological-Trivial' BBH trilayer systems. (a1)-(c1) Below the critical interlayer coupling strength ($t_v = t_c - 1$). (a2)-(c2) Above the critical interlayer coupling strength ($t_v = t_c + 1$). Each band is assigned a number that represents its polarization. Parameters are chosen as $\kappa_1 = 1$ and $\kappa_2 = 3$ for (a) and (b), whereas the values are reversed ($\kappa_1 = 3$ and $\kappa_2 = 1$) for (c).

Fig. 7(a1,a2). The gapping of the Wannier bands results from the non-commutativity of the two reflection symmetries, $\mathcal{M}_x^{\text{bi}}$ and $\mathcal{M}_y^{\text{bi}}$, as discussed in [27]. These two reflection symmetries in the bilayer system are derived from the direct product of the monolayer symmetries, $\mathcal{M}_{x,y}^{\text{mono}}$, expressed as $\mathcal{M}_{x,y}^{\text{bi}} = \mathbb{I}_2 \otimes \mathcal{M}_{x,y}^{\text{mono}}$.

The Wannier bands exhibit distinct structures below and above the critical interlayer coupling strength, t_c^{bilayer} . The nested Wilson loop calculation of the Wannier bands yields band polarizations of $p_y = \{1/2, 0, 0, 1/2\}$ for $t_v < t_c^{\text{bilayer}}$ and $p_y = \{0, 0, 0, 0\}$ for $t_v > t_c^{\text{bilayer}}$. This change in polarization, corresponding with the disappearance of corner states in finite systems, indicates a transition to a strong interlayer coupling regime, reducing the quantized quadrupole moment from one to zero.

The Wilson loop calculation applied to the occupied bands of the trilayer structure in Fig. 1(d), yields six non-degenerate Wannier bands (Fig. 7(b1,b2)). As t_v increases, the Wannier bands experience changes, leading to different polarizations. For $t_v < t_c^{\text{trilayer}}$, we obtain polarizations of $p_y = \{1/2, 1/2, 0, 0, 1/2, 1/2\}$, identifying the phase as trivial even with the existence of corner

states. In contrast, for $t_v > t_c^{\text{trilayer}}$, the polarizations are $p_y = \{1/2, 0, 0, 0, 0, 1/2\}$, indicating a topological phase.

For the alternative trilayer structure depicted in Fig. 1(e), the Wilson loop calculation generates six non-degenerate Wannier bands (Fig. 7(c1,c2)). The nested Wilson loop computation yields polarizations of $p_y = \{1/2, 0, 0, 0, 0, 1/2\}$ for $t_v < t_c^{\text{trilayer}}$ and $p_y = \{0, 0, 0, 0, 0, 0\}$ for $t_v > t_c^{\text{trilayer}}$. These polarization changes correspond with the number of corners obtained in finite-sized system calculations.

APPENDIX C: PERTURBATION THEORY

A numerical simulation shows that there are four corner states at large interlayer couplings t_v in the 'topological-trivial-topological' trilayer structure. In order to understand it, we derive the effective Hamiltonian for large interlayer couplings t_v . We first diagonalize the interlayer coupling Hamiltonian H_0 defined by

$$\mathcal{H}_0 = \begin{pmatrix} 0 & \mathcal{H}_v & 0 \\ \mathcal{H}_v & 0 & \mathcal{H}_v \\ 0 & \mathcal{H}_v & 0 \end{pmatrix}, \quad (19)$$

$$P_0^{-1}U_0^{-1}\mathcal{H}_{\text{trilayer}}U_0P_0 = \begin{pmatrix} 0 & 0 & \kappa_1 + \kappa_2 e^{-ik_x} & \kappa_1 + \kappa_2 e^{ik_y} \\ 0 & 0 & \kappa_1 + \kappa_2 e^{-ik_y} & -(\kappa_1 + \kappa_2 e^{ik_x}) \\ \kappa_1 + \kappa_2 e^{ik_x} & \kappa_1 + \kappa_2 e^{ik_y} & 0 & 0 \\ \kappa_1 + \kappa_2 e^{-ik_y} & -(\kappa_1 + \kappa_2 e^{-ik_x}) & 0 & 0 \end{pmatrix}, \quad (22)$$

where P_0 is a projection operator taking the middle four by four matrix. It is the effective Hamiltonian, which is also the BBH model. Hence, there are four corner modes for large interlayer couplings t_v .

APPENDIX D: CHIRAL SYMMETRIC HAMILTONIAN FOR BBH BILAYER SYSTEM

As an illustrative example, we provide a detailed calculation for $N = 2$ for bilayer systems. The submatrix of BBH bilayer Hamiltonian in equation (6) is composed of four $2N^2 \times 2N^2$ submatrices, described as

$$h_{\text{bilayer}} = \begin{pmatrix} h_{\text{Topo}} & \mathcal{H}_{\text{vp}} \\ \mathcal{H}_{\text{vp}} & h_{\text{Tri}} \end{pmatrix}, \quad (23)$$

where

$$h_{\text{Topo}} = \begin{pmatrix} -\kappa_1 & 0 & 0 & 0 & \kappa_1 & 0 & 0 & 0 \\ -\kappa_2 & -\kappa_1 & 0 & 0 & 0 & \kappa_1 & 0 & 0 \\ 0 & 0 & -\kappa_1 & 0 & \kappa_2 & 0 & \kappa_1 & 0 \\ 0 & 0 & -\kappa_2 & -\kappa_1 & 0 & \kappa_2 & 0 & \kappa_1 \\ \kappa_1 & 0 & \kappa_2 & 0 & \kappa_1 & \kappa_2 & 0 & 0 \\ 0 & \kappa_1 & 0 & \kappa_2 & 0 & \kappa_1 & 0 & 0 \\ 0 & 0 & \kappa_1 & 0 & 0 & 0 & \kappa_1 & \kappa_2 \\ 0 & 0 & 0 & \kappa_1 & 0 & 0 & 0 & \kappa_1 \end{pmatrix}, \quad (24)$$

where only the interlayer coupling exist. It is diagonalized as

$$U_0^{-1}\mathcal{H}_0U_0 = \begin{pmatrix} -\sqrt{2}\mathbb{I}_4 & 0 & 0 \\ 0 & 0 & 0 \\ 0 & 0 & \sqrt{2}\mathbb{I}_4 \end{pmatrix}, \quad (20)$$

where \mathbb{I}_4 is the four by four identical matrix and the transformation matrix U_0 is given by

$$U_0 = \begin{pmatrix} \mathbb{I}_4 & -\sqrt{2}\mathbb{I}_2 \otimes \sigma_x & \mathbb{I}_4 \\ -\mathbb{I}_4 & 0 & \mathbb{I}_4 \\ \mathbb{I}_4 & \sqrt{2}\mathbb{I}_2 \otimes \sigma_x & \mathbb{I}_4 \end{pmatrix}. \quad (21)$$

We are interested in the middle four by four matrix, where there are three degenerate zero energy states in (20). Next, we transform the full Hamiltonian and take the middle four by four matrix, which is given by

and $\mathcal{H}_{\text{vp}} = t_v \times \mathbb{I}_{2N^2}$. Note that h_{Topo} and h_{Tri} have an inverse relationship with respect to the ratio between κ_1 and κ_2 .

For $N = 2$, the sublattice quadrupole moment operator \mathcal{Q}_{xy}^S of the BBH bilayer system is a diagonal matrix where the diagonal elements form a repeating sequence of $(-i, -1, -1, 1)$, this sequence repeats $2N$ times. Thus, $\mathcal{Q}_{xy}^S = \mathbb{I}_4 \otimes \text{diag.}(-i, -1, -1, 1)$.

The calculation process for bilayer systems can be readily extended to trilayer systems. The submatrix of BBH trilayer Hamiltonian is

$$h_{\text{trilayer}} = \begin{pmatrix} h_{\text{Topo}} & \mathcal{H}_{\text{vp}} & 0 \\ \mathcal{H}_{\text{vp}} & h_{\text{Tri}} & \mathcal{H}_{\text{vp}} \\ 0 & \mathcal{H}_{\text{vp}} & h_{\text{Topo}} \end{pmatrix}, \quad (25)$$

The matrix \mathcal{Q}_{xy}^S of the BBH trilayer system is given by $\mathcal{Q}_{xy}^S = \mathbb{I}_6 \otimes \text{diag.}(-i, -1, -1, 1)$ for $N = 2$.

ACKNOWLEDGEMENT

N.I. was supported by the JSPS KAKENHI (Grant No. JP21J40088). M.E. was supported by CREST, JST (Grants No. JPMJCR20T2) and by the Grants-in-Aid for Scientific Research from MEXT KAKENHI (Grant

No.23H00171). Y.O. was supported by the Grants-in-Aid for Scientific Research from MEXT KAKENHI (Grants No.22H01994 and No. 22H00298). S.I. was supported

by CREST, JST (Grant No. JPMJCR19T1) and the Grants-in-Aid for Scientific Research from MEXT KAKENHI (Grants No 22H00298 and No. 22H01994).

-
- [1] M. Z. Hasan and C. L. Kane, Colloquium: Topological insulators, *Rev. Mod. Phys.* **82**, 3045 (2010).
- [2] X.-L. Qi and S.-C. Zhang, Topological insulators and superconductors, *Rev. Mod. Phys.* **83**, 1057 (2011).
- [3] A. Bansil, H. Lin, and T. Das, Colloquium: Topological band theory, *Rev. Mod. Phys.* **88**, 021004 (2016).
- [4] Y. Hatsugai, Chern number and edge states in the integer quantum hall effect, *Phys. Rev. Lett.* **71**, 3697 (1993).
- [5] Y. Hatsugai, Edge states in the integer quantum hall effect and the riemann surface of the bloch function, *Phys. Rev. B* **48**, 11851 (1993).
- [6] T. Ozawa, H. M. Price, A. Amo, N. Goldman, M. Hafezi, L. Lu, M. C. Rechtsman, D. Schuster, J. Simon, O. Zilberberg, and I. Carusotto, Topological photonics, *Rev. Mod. Phys.* **91**, 015006 (2019).
- [7] A. B. Khanikaev, S. Hossein Mousavi, W.-K. Tse, M. Kargarian, A. H. MacDonald, and G. Shvets, Photonic topological insulators, *Nature Materials* **12**, 233 (2013).
- [8] L. Lu, J. D. Joannopoulos, and M. Soljačić, Topological photonics, *Nature Photonics* **8**, 821 (2014).
- [9] Y. Ota, K. Takata, T. Ozawa, A. Amo, Z. Jia, B. Kante, M. Notomi, Y. Arakawa, and S. Iwamoto, Active topological photonics, *Nanophotonics* **9**, 547 (2020).
- [10] S. Iwamoto, Y. Ota, and Y. Arakawa, Recent progress in topological waveguides and nanocavities in a semiconductor photonic crystal platform [invited], *Opt. Mater. Express* **11**, 319 (2021).
- [11] Z. Yang, F. Gao, X. Shi, X. Lin, Z. Gao, Y. Chong, and B. Zhang, Topological acoustics, *Phys. Rev. Lett.* **114**, 114301 (2015).
- [12] C. He, X. Ni, H. Ge, X.-C. Sun, Y.-B. Chen, M.-H. Lu, X.-P. Liu, and Y.-F. Chen, Acoustic topological insulator and robust one-way sound transport, *Nature Physics* **12**, 1124 (2016).
- [13] Y.-G. Peng, C.-Z. Qin, D.-G. Zhao, Y.-X. Shen, X.-Y. Xu, M. Bao, H. Jia, and X.-F. Zhu, Experimental demonstration of anomalous floquet topological insulator for sound, *Nature Communications* **7**, 13368 (2016).
- [14] H. Xue, Y. Yang, and B. Zhang, Topological acoustics, *Nature Reviews Materials* **7**, 974 (2022).
- [15] C. L. Kane and T. C. Lubensky, Topological boundary modes in isostatic lattices, *Nature Physics* **10**, 39 (2014).
- [16] R. Süssstrunk and S. D. Huber, Observation of phononic helical edge states in a mechanical topological insulator, *Science* **349**, 47 (2015).
- [17] S. D. Huber, Topological mechanics, *Nature Physics* **12**, 621 (2016).
- [18] C.-W. Chen, R. Chaunsali, J. Christensen, G. Theocharis, and J. Yang, Corner states in a second-order mechanical topological insulator, *Communications Materials* **2**, 62 (2021).
- [19] H. Hu, S. Han, Y. Yang, D. Liu, H. Xue, G.-G. Liu, Z. Cheng, Q. J. Wang, S. Zhang, B. Zhang, and Y. Luo, Observation of topological edge states in thermal diffusion, *Advanced Materials* **34**, 2202257 (2022).
- [20] M. Ezawa, Higher-order topological electric circuits and topological corner resonance on the breathing kagome and pyrochlore lattices, *Phys. Rev. B* **98**, 201402(R) (2018).
- [21] S. Imhof, C. Berger, F. Bayer, J. Brehm, L. W. Molenkamp, T. Kiessling, F. Schindler, C. H. Lee, M. Greiter, T. Neupert, and R. Thomale, Topoelectrical-circuit realization of topological corner modes, *Nature Physics* **14**, 925 (2018).
- [22] C. H. Lee, S. Imhof, C. Berger, F. Bayer, J. Brehm, L. W. Molenkamp, T. Kiessling, and R. Thomale, Topoelectrical circuits, *Communications Physics* **1**, 39 (2018).
- [23] Y. Li, Y. Sun, W. Zhu, Z. Guo, J. Jiang, T. Kariyado, H. Chen, and X. Hu, Topological lc-circuits based on microstrips and observation of electromagnetic modes with orbital angular momentum, *Nature Communications* **9**, 4598 (2018).
- [24] M. Ezawa, Non-hermitian higher-order topological states in nonreciprocal and reciprocal systems with their electric-circuit realization, *Phys. Rev. B* **99**, 201411(R) (2019).
- [25] G. Harari, M. A. Bandres, Y. Lumer, M. C. Rechtsman, Y. D. Chong, M. Khajavikhan, D. N. Christodoulides, and M. Segev, Topological insulator laser: Theory, *Science* **359**, eaar4003 (2018).
- [26] M. A. Bandres, S. Wittek, G. Harari, M. Parto, J. Ren, M. Segev, D. N. Christodoulides, and M. Khajavikhan, Topological insulator laser: Experiments, *Science* **359**, eaar4005 (2018).
- [27] W. A. Benalcazar, B. A. Bernevig, and T. L. Hughes, Quantized electric multipole insulators, *Science* **357**, 61 (2017).
- [28] W. A. Benalcazar, B. A. Bernevig, and T. L. Hughes, Electric multipole moments, topological multipole moment pumping, and chiral hinge states in crystalline insulators, *Phys. Rev. B* **96**, 245115 (2017).
- [29] M. Ezawa, Higher-order topological insulators and semimetals on the breathing kagome and pyrochlore lattices, *Phys. Rev. Lett.* **120**, 026801 (2018).
- [30] M. Ezawa, Minimal models for wannier-type higher-order topological insulators and phosphorene, *Phys. Rev. B* **98**, 045125 (2018).
- [31] B.-Y. Xie, H.-F. Wang, H.-X. Wang, X.-Y. Zhu, J.-H. Jiang, M.-H. Lu, and Y.-F. Chen, Second-order photonic topological insulator with corner states, *Phys. Rev. B* **98**, 205147 (2018).
- [32] H.-X. Wang, L. Liang, B. Jiang, J. Hu, X. Lu, and J.-H. Jiang, Higher-order topological phases in tunable c3 symmetric photonic crystals, *Photon. Res.* **9**, 1854 (2021).
- [33] M. Lin and T. L. Hughes, Topological quadrupolar semimetals, *Phys. Rev. B* **98**, 241103(R) (2018).
- [34] F. Schindler, A. M. Cook, M. G. Vergniory, Z. Wang, S. S. P. Parkin, B. A. Bernevig, and T. Neupert, Higher-order topological insulators, *Science Advances* **4**, eaat0346 (2018).

- [35] S. H. Kooi, G. van Miert, and C. Ortix, Inversion-symmetry protected chiral hinge states in stacks of doped quantum hall layers, *Phys. Rev. B* **98**, 245102 (2018).
- [36] S. A. A. Ghorashi, T. Li, and T. L. Hughes, Higher-order weyl semimetals, *Phys. Rev. Lett.* **125**, 266804 (2020).
- [37] Q. Wei, X. Zhang, W. Deng, J. Lu, X. Huang, M. Yan, G. Chen, Z. Liu, and S. Jia, 3d hinge transport in acoustic higher-order topological insulators, *Phys. Rev. Lett.* **127**, 255501 (2021).
- [38] N. P. Armitage, E. J. Mele, and A. Vishwanath, Weyl and dirac semimetals in three-dimensional solids, *Rev. Mod. Phys.* **90**, 015001 (2018).
- [39] Y. Ota, F. Liu, R. Katsumi, K. Watanabe, K. Wakabayashi, Y. Arakawa, and S. Iwamoto, Photonic crystal nanocavity based on a topological corner state, *Optica* **6**, 786 (2019).
- [40] X.-D. Chen, W.-M. Deng, F.-L. Shi, F.-L. Zhao, M. Chen, and J.-W. Dong, Direct observation of corner states in second-order topological photonic crystal slabs, *Phys. Rev. Lett.* **122**, 233902 (2019).
- [41] M. Li, D. Zhirihin, M. Gorlach, X. Ni, D. Filonov, A. Slobozhanyuk, A. Alù, and A. B. Khanikaev, Higher-order topological states in photonic kagome crystals with long-range interactions, *Nature Photonics* **14**, 89 (2020).
- [42] D. Smirnova, A. Tripathi, S. Kruk, M.-S. Hwang, H.-R. Kim, H.-G. Park, and Y. Kivshar, Room-temperature lasing from nanophotonic topological cavities, *Light: Science & Applications* **9**, 127 (2020).
- [43] W. Zhang, X. Xie, H. Hao, J. Dang, S. Xiao, S. Shi, H. Ni, Z. Niu, C. Wang, K. Jin, X. Zhang, and X. Xu, Low-threshold topological nanolasers based on the second-order corner state, *Light: Science & Applications* **9**, 109 (2020).
- [44] H.-R. Kim, M.-S. Hwang, D. Smirnova, K.-Y. Jeong, Y. Kivshar, and H.-G. Park, Multipolar lasing modes from topological corner states, *Nature Communications* **11**, 5758 (2020).
- [45] M. S. Kirsch, Y. Zhang, M. Kremer, L. J. Maczewsky, S. K. Ivanov, Y. V. Kartashov, L. Torner, D. Bauer, A. Szameit, and M. Heinrich, Nonlinear second-order photonic topological insulators, *Nature Physics* **17**, 995 (2021).
- [46] M. Ezawa, Nonlinear non-hermitian higher-order topological laser, *Phys. Rev. Res.* **4**, 013195 (2022).
- [47] X. Xie, W. Zhang, X. He, S. Wu, J. Dang, K. Peng, F. Song, L. Yang, H. Ni, Z. Niu, C. Wang, K. Jin, X. Zhang, and X. Xu, Cavity quantum electrodynamics with second-order topological corner state, *Laser & Photonics Reviews* **14**, 1900425 (2020).
- [48] E. Kim, X. Zhang, V. S. Ferreira, J. Banker, J. K. Iverson, A. Sipahigil, M. Bello, A. González-Tudela, M. Mirhosseini, and O. Painter, Quantum electrodynamics in a topological waveguide, *Phys. Rev. X* **11**, 011015 (2021).
- [49] C.-A. Li, S.-B. Zhang, J. Li, and B. Trauzettel, Higher-order Fabry-Pérot interferometer from topological hinge states, *Phys. Rev. Lett.* **127**, 026803 (2021).
- [50] A. Y. Chaou, P. W. Brouwer, and N. Sedlmayr, Hinge states of second-order topological insulators as a mach-zehnder interferometer, *Phys. Rev. B* **107**, 035430 (2023).
- [51] A. M. Cook and A. E. B. Nielsen, Finite-size topology, *Phys. Rev. B* **108**, 045144 (2023).
- [52] R. Flores-Calderon, R. Moessner, and A. M. Cook, Time-reversal invariant finite-size topology, *Phys. Rev. B* **108**, 125410 (2023).
- [53] A. M. C. Michał J. Pacholski, Crystalline finite-size topology, arXiv:2312.08552 (2023).
- [54] S. Mittal, V. V. Orre, G. Zhu, M. A. Gorlach, A. Poddubny, and M. Hafezi, Photonic quadrupole topological phases, *Nature Photonics* **13**, 692 (2019).
- [55] J. Schulz, J. Noh, W. A. Benalcazar, G. Bahl, and G. von Freymann, Photonic quadrupole topological insulator using orbital-induced synthetic flux, *Nature Communications* **13**, 6597 (2022).
- [56] M. Serra-Garcia, V. Peri, R. Süsstrunk, O. R. Bilal, T. Larsen, L. G. Villanueva, and S. D. Huber, Observation of a phononic quadrupole topological insulator, *Nature* **555**, 342 (2018).
- [57] C. W. Peterson, W. A. Benalcazar, T. L. Hughes, and G. Bahl, A quantized microwave quadrupole insulator with topologically protected corner states, *Nature* **555**, 346 (2018).
- [58] W. A. Benalcazar and A. Cerjan, Chiral-symmetric higher-order topological phases of matter, *Phys. Rev. Lett.* **128**, 127601 (2022).
- [59] D. Wang, Y. Deng, J. Ji, M. Oudich, W. A. Benalcazar, G. Ma, and Y. Jing, Realization of a \mathbb{Z} -classified chiral-symmetric higher-order topological insulator in a coupling-inverted acoustic crystal, *Phys. Rev. Lett.* **131**, 157201 (2023).
- [60] Y. Li, J.-H. Zhang, F. Mei, B. Xie, M.-H. Lu, J. Ma, L. Xiao, and S. Jia, Large-chiral-number corner modes in \mathbb{Z} -class higher-order topoelectrical circuits, *Phys. Rev. Appl.* **20**, 064042 (2023).
- [61] Y. Qi, Z. He, K. Deng, J. Li, and Y. Wang, Multipole higher-order topological semimetals, *Phys. Rev. B* **109**, L060101 (2024).
- [62] W.-J. Yang, S.-F. Li, X.-Y. Zou, and J.-C. Cheng, Characterization of zero-energy corner states in higher-order topological systems with chiral symmetry, *Phys. Rev. B* **109**, 024114 (2024).
- [63] L. Lin, Y. Ke, and C. Lee, Real-space representation of the winding number for a one-dimensional chiral-symmetric topological insulator, *Phys. Rev. B* **103**, 224208 (2021).
- [64] W. A. Wheeler, L. K. Wagner, and T. L. Hughes, Many-body electric multipole operators in extended systems, *Phys. Rev. B* **100**, 245135 (2019).